

A statistical study of multiply-imaged systems in the lensing cluster Abell 68.^{1,2}

Johan Richard³, Jean-Paul Kneib^{3,4}, Eric Jullo^{5,4}, Giovanni Covone⁶, Marceau Limousin⁷, Richard Ellis³, Daniel Stark³, Kevin Bundy³, Oliver Czoske⁸, Harald Ebeling⁹ and Geneviève Soucail¹⁰

ABSTRACT

We have carried out an extensive spectroscopic survey with the Keck and VLT telescopes, targeting lensed galaxies in the background of the massive cluster Abell 68. Spectroscopic measurements are obtained for 26 lensed images, including a distant galaxy at $z = 5.4$. Redshifts have been determined for 5 out of 7 multiply-image systems. Through a careful modeling of the mass distribution in the strongly-lensed regime, we derive a mass estimate of $5.3 \times 10^{14} M_{\odot}$ within 500 kpc. Our mass model is then used to constrain the redshift distribution of the remaining multiply-imaged and singly-imaged sources. This enables us to examine the physical properties for a subsample of 7 Lyman- α emitters at $1.7 \lesssim z \lesssim 5.5$, whose unlensed luminosities of $\simeq 10^{41}$ ergs s⁻¹ are fainter than similar objects found in blank fields. Of particular interest is an extended Lyman- α emission region surrounding a highly magnified source at $z = 2.6$, detected in VIMOS Integral Field Spectroscopy data. The physical scale of the most distant lensed source at $z = 5.4$ is very small (< 300 pc), similar to the lensed $z \sim 5.6$ emitter reported by Ellis et al. (2001) in Abell 2218. New photometric data available for Abell 2218 allow for a direct comparison between these two unique objects. Our survey illustrates the practicality of using lensing clusters to probe the faint end of the $z \sim 2 - 5$ Lyman- α luminosity function in a manner that is complementary to blank field narrow-band surveys.

Subject headings: cosmology: observations — galaxies: clusters: individual (A68) — gravitational lensing — galaxies: high redshift

¹Data presented herein were obtained at the W.M. Keck Observatory, which is operated as a scientific partnership among the California Institute of Technology, the University of California and the National Aeronautics and Space Administration. The Observatory was made possible by the generous financial support of the W.M. Keck Foundation.

²Also based on observations collected at the Very Large Telescope (Antu/UT1 and Melipal/UT3), European Southern Observatory, Paranal, Chile (ESO Programs 070.A-0643, 073.A-0774), the NASA/ESA *Hubble Space Telescope* (Program #8249) obtained at the Space Telescope Science Institute, which is operated by AURA under NASA contract NAS5-26555, and the Canada-France-Hawaii Telescope.

³Department of Astronomy, California Institute of Technology, 105-24, Pasadena, CA91125; (johan,kneib,dps,rse,kbundy)@astro.caltech.edu

⁴OAMP, Laboratoire d'Astrophysique de Marseille UMR 6110 Traverse du Siphon 13012 Marseille, France; Jean-Paul.Kneib@oamp.fr

⁵European Southern Observatory, Alonso de Cordova 3107, Vitacura, Chile; ejullo@eso.org

⁶INAF - Osservatorio Astronomico di Capodimonte, Salita Moiariello, 16, 80131 Napoli, Italy; giovanni.covone@na.astro.it

⁷Dark Cosmology Centre - Niels Bohr Institute, University of Copenhagen, Juliane Maries Vej 30, DK-2100 Copenhagen; marceau@dark-cosmology.dk

⁸Argelander-Institut für Astronomie (Founded by merging of the Institut für Astrophysik und Extraterrestrische Forschung, the Sternwarte, and the Radioastronomisches Institut der Universität Bonn), Universität Bonn, Auf dem Hügel 71, 53121 Bonn, Germany; oczoske@astro.uni-bonn.de

⁹Institute of Astronomy, University of Hawaii, 2680 Woodlawn Drive, Honolulu, HI 96822; ebeling@ifa.hawaii.edu

¹⁰Observatoire Midi-Pyrénées, UMR5572, 14 Avenue Edouard Belin, 31000 Toulouse, France; soucail@ast.obs-mip.fr

1. Introduction

The central regions of massive galaxy clusters act as powerful *gravitational telescopes*, magnifying the light from background galaxies via the effect of strong lensing. Such magnifications can attain typical values of 1 to 3 magnitudes in concentrated cluster cores, enabling the detection of intrinsically fainter sources than in unlensed field surveys. The detailed study of low luminosity galaxies at $z > 2$, where the major fraction of star-formation activity is thought to occur, is an interesting but poorly-understood topic. Such galaxies can either be found through their Lyman- α emission (e.g., Franx et al. 1997; Santos et al. 2004), or through their ultraviolet continuum fluxes via the Lyman break techniques (Kneib et al. 2004; Richard et al. 2006).

A prerequisite for strong lensing studies of intrinsically faint galaxies at high redshift is an accurate measurement of the projected mass distribution in the lens (Kneib et al. 2003; Gavazzi et al. 2003; Sand et al. 2005). Such mass models are primarily limited by the number of available multiply-imaged sources of known redshift. Only a few well-studied clusters like Abell 1689 (Broadhurst et al. 2005; Halkola et al. 2006; Limousin et al. 2007), with more than 30 multiply-imaged systems, or Abell 2218 (Ebbels et al. 1996; Kneib et al. 1996) have sufficient constraints to permit precise modelling of each individual dark matter clump.

Spectroscopic searches for Lyman- α emitters (LAEs) at high redshift usually have a better line flux sensitivity and span a larger redshift range ($\Delta z \sim 4$) than those of wide-field narrow-band surveys. This gain in sensitivity is even larger in strong lensing applications. Lensed spectroscopic surveys may also be sensitive to sources with emission lines with an equivalent width $W < 20 \text{ \AA}$, smaller than those in narrow-band surveys (e.g., Fynbo et al. 2003; Shimasaku et al. 2006). An additional complication in narrow-band surveys is how interlopers are treated; confirmatory spectroscopy is usually necessary. By contrast, in lensed surveys, the geometrical configuration of multiply-imaged systems can reliably distinguish between high redshift objects and low redshift interlopers (see e.g., Ellis et al. 2001).

As our surveys expand, a variety of types of emission line galaxies are being discovered. Of particular interest are the extended Lyman- α emission sources which have been mainly discovered in regions of significant overdensity through deep narrow-band imaging (Steidel et al. 2000; Francis et al. 2001). Matsuda et al. (2004) have identified a large number of such giant Lyman- α *blobs* (with a typical size $> 50 \text{ kpc}$) in a $34' \times 27'$ field of view, demonstrating the existence of a continuous distribution. The origin of the extended Lyman- α emission in such radio-quiet sources may be explained by gas inflow during the early stages of galaxy formation: large amounts of hydrogen collapsing into the dark matter potential well will cool through Lyman- α radiation. Giant Lyman- α blobs may thus be the progenitors of very massive galaxies in the local Universe. A key issue is whether the same process is seen to occur in lower-mass objects. A route to addressing this question is to examine the nature of smaller extended Lyman- α sources, either by long-slit or Integral Field Spectroscopy (IFS). This identification is more easily accomplished in strongly-lensed sources where magnification will stretch the observed physical scales.

The spatial magnification associated with lensing can also be used to yield physical sizes for the most distant sources. Using strong lensing in the cluster Abell 2218, Ellis et al. (2001) located a remarkably small source at $z=5.6$ where the combination of the Ly α emission line flux density and the weak stellar continuum were used to deduce a young age and modest stellar mass ($\simeq 10^{6-7} M_{\odot}$) consistent, perhaps, with a forming globular cluster. Further surveys are required to evaluate whether such systems are common at $z \simeq 6$.

The major drawback arising from the study of lensed sources located through studies of individual clusters is, of course, the significant cosmic variance that is associated with the small volumes being probed.

Compared to field surveys, any statistical inferences on the abundances of various classes of populations may be much more uncertain, even granting fainter sources are probed. To overcome this limitation, an effective survey would have to be conducted through a large sample ($\simeq 20\text{--}40$) of lensing clusters, each with reliable mass models based on the spectroscopic study of many multiply-imaged systems (Kneib et al. 1996). Fortunately, the construction of such a sample of well-mapped clusters is now a realistic proposition. Several Hubble Space Telescope (HST) snapshot imaging surveys of X-ray luminous clusters are now underway with associated ground-based spectroscopy, such as the MAssive Clusters Survey (MACS, GO#10491, P.I.: H. Ebeling) and the Local Cluster Substructure Survey (LoCuSS, GO#10881, P.I.: G. Smith).

The purpose of this paper is to illustrate the promise of such surveys by examining spectroscopically the rich population of lensed sources located in the lensing cluster Abell 68 ($\alpha=00:37:06.81$ $\delta=+09:09:24.0$ J2000, $z = 0.255$), one of the most X-ray luminous clusters ($L_X \sim 8.4 \pm 2.3 \times 10^{44} \text{ erg s}^{-1}$, 0.1–2.4 keV) in the X-ray Brightest Abell-type Clusters sample (XBACS, Ebeling et al. (1996)). Strong lensing in this cluster has been previously studied by Smith et al. (2005), hereafter S05, as part of a survey of 10 X-ray luminous galaxy clusters at $z \sim 0.2$. Smith et al identified a list of potential multiple-image systems, a few of which were confirmed spectroscopically. Here we significantly extend this work by securing the redshifts of new multiple-image systems, many of which are strongly-lensed Lyman- α emitters at $z \gtrsim 2$. The combination of a large magnification factor, high-resolution HST imaging and broad-band photometry enables us to demonstrate the value of studying the physical properties of these faint emitters, such as their star formation rates, intrinsic scales and stellar masses. The paper is intended to illustrate the significant promise of continuing such spectroscopic work with the larger samples of clusters now being surveyed with HST.

The paper is organized as follows. In Section 2, we describe the various observations and the reduction of the spectroscopic data. We present in Section 3 the strong-lensing constraints, in the light of the redshifts and identification of new multiply-imaged systems. Section 4 presents a mass model of the cluster from which the source magnifications are deduced. The physical properties of the various categories of high redshift LAEs are presented in Section 5 and the implications are discussed in the context of the limitations of blank field surveys in Section 6. We summarize our conclusions in Section 7.

Throughout this paper, we adopt the following cosmology: a flat Λ -dominated Universe with the values $\Omega_\Lambda = 0.7$, $\Omega_m = 0.3$, $\Omega_b = 0.045$ and $H_0 = 70 \text{ km s}^{-1} \text{ Mpc}^{-1}$. All magnitudes given in the paper are quoted in the AB system (Oke 1974). The correction values C_{AB} between AB and Vega photometric systems, defined as $m_{AB} = m_{\text{Vega}} + C_{AB}$, are reported in Table 1 for each filter. At the redshift $z = 0.255$ of the cluster, the angular diameter distance is $3.9 \text{ kpc arcsec}^{-1}$.

2. Observations and Data Reduction

We present in this section the photometric and spectroscopic datasets used to assemble our catalog. High resolution images are crucial for the morphological identification of multiple image systems and the precise astrometric position of the sources studied here, whereas multicolor images are used to estimate their spectral energy distributions. Redshift and emission lines measurements for individual objects were obtained during subsequent spectroscopic observations. These included multi-object spectroscopy of multiply-imaged candidates, as well as systematic long-slit searches in the central regions of the cluster. Figure 1 shows the location of the main spectroscopic settings in the cluster field.

2.1. Imaging data

A considerable body of multi-wavelength data exists in the field around Abell 68, including high resolution HST imaging. The main characteristics of the dataset used in this study are summarized in Table 1. 3×2.5 ks of integration time with the Wide Field Planetary Camera (WFPC2) was obtained during Cycle 8 in the R -F702W band, as part of HST program #8249 (PI : J.P. Kneib). Observations were carried out in low sky mode, and a $1.0''$ dithering pattern was used between each exposure. Details on the reduction of these data are given in S05.

Recognition of faint multiply-imaged systems in the vicinity of the cluster core is hindered by the dominant stellar halo of the Brightest Cluster Galaxy (BCG). To overcome this, we fitted and subtracted from the HST image a model representation of the surface brightness distribution using the IRAF task `ellipse`. Both the position angle and ellipticity were allowed to vary as a function of the semimajor axis in the fitted elliptical isophotes, as well as the isophote centroid in the central part. This procedure was found to give satisfactory residuals at the center (Figure 3).

Associated optical images in B, R, I have been obtained on UT 1999 November 19 using the CFH12k camera at CFHT. These sample a field of $42' \times 28'$ at a $0.205''$ pixel scale. The total exposure times are 8.1, 7.2 and 3.6 ks in the B, R and I band, respectively. The data was reduced using procedures similar to those described by Czoske (2002) and Bardeau et al. (2005).

At longer wavelengths, Abell 68 has been observed at the Very Large Telescope using the FOcal Reducer / low dispersion Spectrograph (FORS2/UT4) in the z -band on UT 2002 October 06, and the Infrared Spectrometer And Array Camera (ISAAC/UT1) in the J and H bands on UT 2002 September 29 . The field of view of the FORS2 image is 7.2×7.2 arcmins after dithering, with a pixel size of $0.252''$, and we used 80 dithered exposures of 120 s. The field of view of the ISAAC images is about 2.5×2.5 arcmins after dithering, with a pixel size of $0.148''$, the subintegration \times integration times of the dithered exposures were 6×35 s and 10×12 s in the J and H bands, respectively. All these data have been reduced using procedures similar to those described by Richard et al. (2006).

Instrument	Filter	Exposure Time (ks)	Pixel Size "	Depth AB mag.	C_{AB} mag.	Seeing "
CFH12k	B	8.1	0.206	27.4	-0.066	1.11
CFH12k	R	7.2	0.206	27.2	0.246	0.67
WFPC2	R_{702W}	7.5	0.1	28.0	0.299	0.17
CFH12k	I	3.6	0.206	26.5	0.462	0.58
FORS2	z	9.6	0.252	26.5	0.554	0.71
ISAAC	J	6.48	0.148	26.2	0.945	0.48
ISAAC	H	7.12	0.148	26.3	1.412	0.48

Table 1: Properties of the photometric dataset: from left to right: instrument and filter names, total integration time, pixel size, photometric depth (defined as 4 pixels above 3σ , where σ stands for the typical local background noise), photometric correction C_{AB} between AB and Vega systems, seeing measured on bright unsaturated stars.

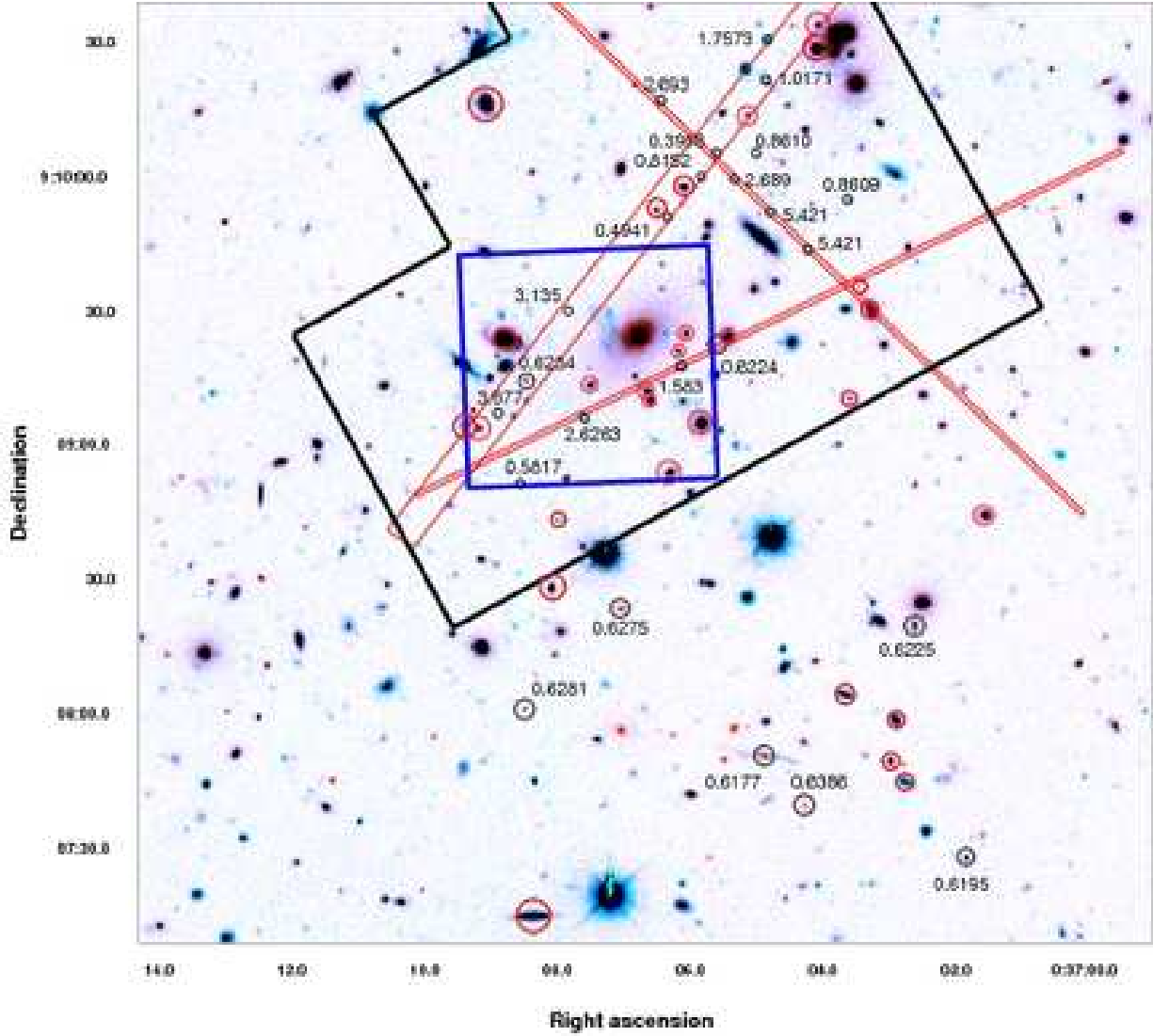


Fig. 1.— Composite CFH12k-*BRI* color image of the field of view around the center of Abell 68. We overplot the redshift measurements obtained for galaxies located in the background of the cluster (black labels). Red circles represent cluster members confirmed with spectroscopy. We delineate the imprints of the HST/WFPC2 (black polygon) and the VIMOS/IFU (blue square) fields, as well as the spatial coverage of the different LRIS long-slit configurations (red rectangles).

2.2. Keck Multi-Object Spectroscopy

The Low Resolution Imaging Spectrograph (LRIS; Oke et al. (1995)) on Keck I has been used in multi-object (MOS) mode during two observing runs, in order to target background galaxies and multiply-imaged candidates selected on the basis of morphology and colors.

On UT 2001 August 4, 4 exposures of 1.8 ks were acquired with a 31 slits-mask, using a 300 l mm^{-1} grism blazed at 5000 \AA in the single red channel of the camera, which covers the approximate range $5500\text{--}9900 \text{ \AA}$ at the dispersion of 2.5 \AA per pixel. The average seeing was $\sim 1.0''$. The night was photometric and spectrophotometric standard stars were used for flux calibration.

On UT 2002 November 30, a 32 slits-mask was used during 3×2.4 ks of integration time. A 6800 \AA dichroic separated the red channel of the instrument, equipped with a 600 l mm^{-1} grating blazed at 7500 \AA , from the blue channel equipped with a 400 l mm^{-1} blazed at 3400 \AA . The whole setting covers the wavelength range $3500\text{--}9500 \text{ \AA}$ with dispersions of 1.28 and 1.09 \AA per pixel in the red and blue channels, respectively. Despite good seeing conditions ($\sim 0.8''$), the night was not photometric and no standard stars were observed.

These datasets were reduced using standard IRAF procedures for bias removal, flat-fielding, wavelength and flux calibration, sky subtraction and extraction of the one-dimensional spectra.

2.3. Keck long-slit spectroscopy

2.3.1. Optical spectroscopy

Abell 68 was observed on UT 2002 September 11 with LRIS, in the course of a survey targeting low-luminosity Lyman- α sources at high redshift (Santos et al. 2004). A $175''$ -long and $1''$ -wide slit was used to map the high magnification regions of a sample of $z \sim 0.2$ lensing clusters. In the case of Abell 68, 6 adjacent slit settings scanned the theoretical location of the critical lines at $z \sim 5$, with 2×1000 s of integration time at each position. The reduction of these data is detailed in (Santos et al. 2004).

In addition to the detection of high redshift sources through their Lyman- α emission, this *blind* spectroscopic survey provided secure redshifts for a number of lensed background galaxies serendipitously falling into the long slit.

On UT 2003 August 26, a single long-slit LRIS position was aligned on two components of a triply-imaged system, discovered as R-dropouts by a *RIz* color-color selection technique (see Sect. 3). A 300 l mm^{-1} grism blazed at 5000 \AA and a 600 l mm^{-1} grating blazed at $1 \mu\text{m}$ were used in the blue and red channels of the instrument, both lightpaths being separated by a dichroic at 6800 \AA . Two exposures of 1.2 ks were acquired at this position, with a $5''$ dithering offset along the slit.

Finally, an additional LRIS long-slit integration of 3×1.2 ks was acquired on UT 2005 November 29 with a 600 l mm^{-1} grism blazed at 4000 \AA , a 400 l mm^{-1} grating blazed at 8500 \AA , a 5600 \AA dichroic, and $5''$ dithering offsets.

2.3.2. Near Infrared Spectroscopy

Abell 68 was observed on UT 2005 October 13 using the Near InfraRed SPECTrograph (NIRSPEC, McLean et al. (1998)) on Keck II, during a spectroscopic survey of the critical lines of lensing clusters similar to the LRIS survey described before, but at longer wavelengths (Stark & Ellis 2006). A $42'' \times 0.76''$ long slit was used at 2 adjacent slit positions, with 9×600 s of integration time on each of them. The spectra were reduced using IDL routines, following optimal spectroscopic reductions techniques presented in Kelson (2003). More details are presented in a forthcoming paper (Stark et al. 2006b, in press).

2.4. VLT - Integral Field Spectroscopy

Abell 68 was observed on UT 2004 August 12 using the VISIBLE Multi-Object Spectrograph (VIMOS, Le Fèvre et al. (2003)) on VLT/UT3 in low-resolution (LR-Blue grism) Integral Field Spectroscopy mode, as part of a survey targeting the central regions of an intermediate-redshift galaxy cluster sample (073.A-0774, PI: Soucail). The $54'' \times 54''$ field of view of the Integral Field Unit (IFU, composed of 6400 fibers, splitted in 4 quadrants feeding the 4 VIMOS CCDs) was centered on the cD galaxy. In the given configuration, the spectral resolution is about 200 and the diameter of the fibers is $0.66''$, covering the wavelength range 3900-6800 Å with a dispersion of 5.355 Å per pixel. 2×2.4 ks of integration time have been acquired without dithering.

These 3D spectroscopic data have been reduced using the Vimos Interactive Pipeline Graphical Interface (VIPGI, Scodreggio et al. 2005)¹. Before building the data cube for each exposure, every step in the data reduction was performed on a single quadrant basis. After bias subtraction and cosmic ray removal (see Zanichelli et al. (2005) for a description of the algorithm), the spectra were traced on the CCDs with the help of the high S/N spectra of a continuum lamp. Following wavelength calibration, inhomogeneities in fiber efficiencies were corrected by measuring the counts in the 5577 Å sky emission line after subtracting the contribution from a galaxy spectrum where fibers cover a galaxy position. The flux-calibration is applied by using observations of a standard star in each quadrant. See Covone et al. (2006), who present similar data on Abell 2667, for a detailed description of the procedures.

2.5. Redshift measurements

We attempted to measure the redshift of all individual objects falling in the slits that revealed a discernable continuum or possible emission lines. To obtain an accurate redshift measurement for foreground galaxies, cluster members and other bright objects, we applied the IRAF task `xcsao` from the Radial Velocity package RVSAO (Kurtz et al. 1992) on all extracted spectra. This procedure uses a cross-correlation method based on spectral templates (Coleman et al. 1980; Kinney et al. 1996) to estimate the redshift and the corresponding redshift error. For the remaining objects in the spectroscopic catalog, the redshift measurement is based on the wavelength at the peak of the brightest emission line detected. In the latter case, we estimated the redshift error from the spectral dispersion. Additional uncertainties generated by the accuracy of the relative and absolute wavelength calibrations, of about 0.8 and 1.5 Å respectively for the LRIS data, were

¹VIPGI has been developed within the VIRMOS Consortium. For more information, see <http://cosmos.mi.iasf.cnr.it/pandora/vipgi.html>

ID	RA 00:	Dec 09:	R [mag]	z	C	Features	μ [mag]	W_0 [Å]
1 (C15a)	37:04.297	09:43.40	26.00 ± 0.18	5.421 ± 0.0021	9	$Ly\alpha$	2.74 ± 0.08	53 ± 16^a
2 (C15b)	37:04.861	09:51.78	26.52 ± 0.22	5.421 ± 0.0021	9	$Ly\alpha$	2.89 ± 0.07	
3 (C26)	37:08.960	09:06.90	27.24 ± 0.25	3.677 ± 0.0022	9	$Ly\alpha$	2.06 ± 0.03	107 ± 8.2
4 (C23a)	37:07.902	09:29.80	26.44 ± 0.18	3.135 ± 0.0021	9	$Ly\alpha$	2.47 ± 0.07	25.9 ± 5.2
5 (C25)	37:06.506	10:16.70	24.40 ± 0.07	2.6930 ± 0.0021	9	$Ly\alpha$	1.12 ± 0.07	10.4 ± 5.1
6 (C20c)	37:05.405	09:59.14	25.15 ± 0.09	2.6890 ± 0.0020	9	$Ly\alpha$	3.61 ± 0.09	30.4 ± 6.3
7 (C4)	37:07.657	09:05.90	23.31 ± 0.04	2.6280 ± 0.0021	9	$Ly\alpha$	4.15 ± 0.16	42.4 ± 2.3
8 (C27)	37:04.906	10:30.20	22.81 ± 0.03	1.7546 ± 0.0021	4	$Ly\alpha$	1.72 ± 0.10	2.4 ± 0.5
9 (C1a)	37:06.207	09:17.49	24.02 ± 0.04	1.5836 ± 0.0011	4	$[O_{III}]$, $H\beta$	2.52 ± 0.06	< 50
10 (C12)	37:04.930	10:21.40	21.67 ± 0.02	1.0171 ± 0.0011	3	$[O_{II}]$, $H\alpha$	1.63 ± 0.06	10.5 ± 1.4
11 (C7)	37:05.073	10:04.90	22.78 ± 0.03	0.8610 ± 0.0007	3	$[O_{II}]$	1.59 ± 0.02	21.3 ± 5.9
12 (C8)	37:03.700	09:54.10	23.08 ± 0.02	0.8609 ± 0.0008	4	$[O_{II}]$	1.37 ± 0.03	112.8 ± 5.1
13 (C24)	37:05.900	09:59.70	23.64 ± 0.02	0.8152 ± 0.0007	1	K, H, $H\gamma$	1.33 ± 0.01	N/A
14	37:04.352	07:39.60	21.91 ± 0.03	0.6386 ± 0.0007	3	$[O_{II}]$	0.10	14.1 ± 4.5
15	37:08.541	08:01.30	22.49 ± 0.03	0.6281 ± 0.0006	3	K, H	0.20	< 10
16	37:07.100	08:23.10	21.44 ± 0.02	0.6275 ± 0.0006	3	K, H	0.28	14.6 ± 2.2
17 (C14)	37:08.534	09:14.10	22.02 ± 0.02	0.6234 ± 0.0007	2	K, H	0.93 ± 0.01	16.5 ± 7.4
18	37:02.707	08:19.18	20.52 ± 0.02	0.6225 ± 0.0006	3	K, H	0.20	6.7 ± 1.3
19	37:05.505	09:24.24	22.71 ± 0.02	0.6224 ± 0.0006	4	$[O_{II}]$, $[O_{III}]$	1.83	25.3 ± 6.5
20	37:01.890	07:27.70	21.40 ± 0.03	0.6195 ± 0.0005	4	Mg_{II} , $[O_{III}]$	0.10	N/A
21	37:05.000	07:50.60	20.33 ± 0.02	0.6177 ± 0.0007	4	$[O_{II}]$	0.10	10.7 ± 1.7
22	37:01.400	05:55.20	22.10 ± 0.02	0.5944 ± 0.0005	4	$H\beta$, $[O_{III}]$	0.0	N/A
23	37:08.620	08:51.40	23.29 ± 0.04	0.5817 ± 0.0006	4	$H\beta$, $[O_{III}]$	0.51	< 10
24	37:06.410	09:50.65	24.66 ± 0.05	0.4941 ± 0.0006	4	$H\beta$, $[O_{III}]$	0.75	< 10
25	37:05.670	10:04.90	24.00 ± 0.04	0.3958 ± 0.0007	4	$H\alpha$, $[O_{III}]$, $[O_{II}]$	0.51	24.5 ± 2.2
26	36:57.170	07:00.80	21.03 ± 0.01	0.3693 ± 0.0005	4	$[O_{II}]$, $[O_{III}]$	0.0	10.2 ± 2.1

Table 2: Spectroscopic catalog of lensed background galaxies. From left to right: astrometric position (J2000), R -band magnitude in AB system (WFPC/F702W, or CFH12k (in italic)), spectroscopic redshift, redshift confidence class (see text for details), main spectroscopic features, magnification factor (in magnitudes), rest-frame equivalent width of Lyman- α (top half) or $[O_{II}]$ emission lines (bottom half).

^aMeasured on the averaged spectrum of C15a and C15b

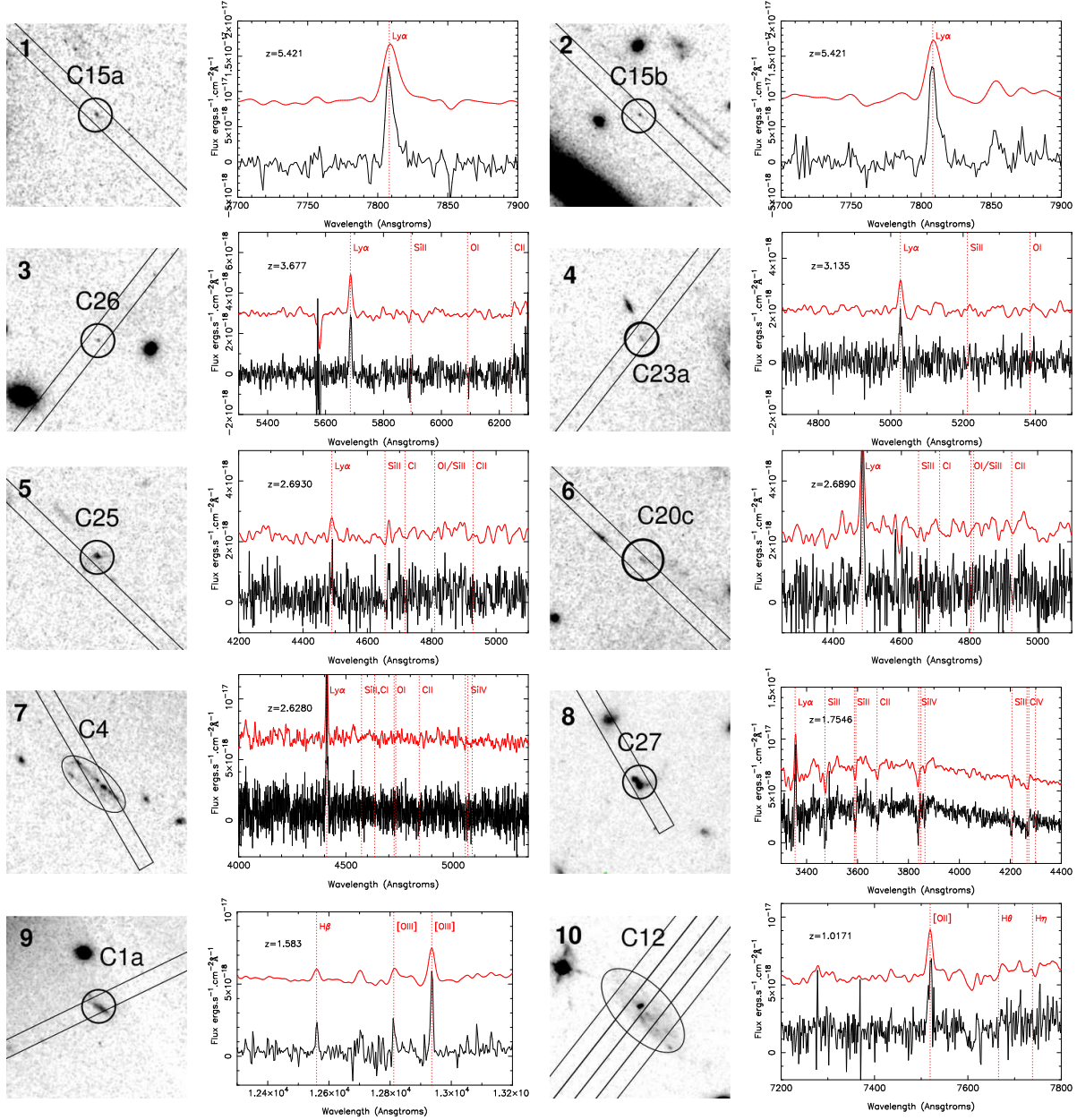


Fig. 2.— $10'' \times 10''$ WFPC/F702W zoomed images with the slit location and extracted spectra for all individual $z > 1$ sources. Dotted lines outline the emission and absorption features identified in each spectrum. Upper red spectra have been smoothed using a $\sigma = 3$ pixels gaussian, and shifted in the vertical direction for clarity.

quadratically added to the previous estimates to yield the final redshift errors.

A confidence class C , ranging from 1 to 4 was assigned to each individual redshift measurement according to the prescription of Le Fèvre et al. (1995): this corresponds to a probability level for a correct identification of 50, 75, 95 and 100%, respectively. A specific value of 9 is used when only a single secure spectral feature is seen in emission. The identification of most $z > 2$ objects in the catalog is based on only a single emission line interpreted as Lyman- α and a confidence class of 9. However, the constraints provided by the lensing configuration in case of multiple images (see Sect. 3) enable us to strengthen most of these interpretations.

Multicolor photometry was performed for all sources identified in the WFPC/F702W band and CFH12k- R band images, using the *SExtractor* software (Bertin & Arnouts 1996). Total magnitudes and errors were measured on the original images without any resampling or convolution.

The final spectroscopic catalog of lensed galaxies is presented in Table 2.

Figure 1 displays the location of all sources in the catalog and the spectroscopic configuration of each dataset. A red circle marks the location of 44 cluster members from our sample, for which we measured a spectroscopic redshift. Long-slit and IFU pointings were mainly focused on the central region of the cluster (within $\sim 80''$), in the vicinity of the critical curves, whereas MOS surveys with LRIS probed a wider field of view of $\sim 6 \times 8$ arcmin.

The redshift distribution of lensed background galaxies appears to be highly correlated. Three sources are located in the $2.63 < z < 2.69$ range, two sources have $z \sim 0.86$, and C1 system has a $z \sim 1.6$ redshift similar to C0 Smith et al. (2002b). Even more prominent is a group of 8 sources having $0.62 < z < 0.64$, which lie predominantly at the south of the cluster center, and exhibit similar colors in the composite CFH12k image (Figure 1).

3. Catalog of Multiply-Imaged Systems

In this section we update the catalog of multiply-imaged systems in the field of Abell 68, taking into account both our new spectroscopic measures and systems without spectroscopy located on the basis of their geometrical location and similar colors. For each system, we present a close-up view from the HST- R image in the bottom panels of Figure 3, and summarize the position, photometry, shape parameters and magnification in Table 3.

3.1. Morphological Identification

Multiply-imaged systems can be identified via a visual inspection of morphologies in the central region of the HST- R_{702W} image (Fig. 3), examined in combination with the broad-band photometric catalogs. Our starting point is a detailed study of candidates identified to $\mu_{702} \sim 25$ mag arcsec $^{-2}$ presented by S05. This work revealed 3 main systems (C0a,b,c; C1a,b,c; C2a,b) as well as 20 other possible multiply-imaged candidates (C3 to C22). We adopt the same nomenclature, extending to include the new systems presented here.

The three images identified as C15, C16 and C17 have been selected as R -band dropouts on the basis of color-color diagrams combining R , I and z -band filters. Indeed, they are very faint in the HST image ($R_{702} \sim 25.7$), undetected at shorter wavelengths in the B or R band with CFH12k with a combination

System	RA 00:	DEC 09:	a "	b "	θ [deg.]	R [mag]	z	μ [mag]
C0 a	37:07.426	09:28.42	0.66	0.33	24.1	25.72±0.10	1.6 ^a	3.14±0.06
b	37:07.324	09:24.03	0.63	0.36	8.1	25.20±0.08		2.72±0.06
c	37:06.161	09:08.84	0.42	0.30	82.3	25.84±0.10		2.15±0.11
radial	37:06.870	09:25.51	0.61	0.19	350.0	26.51±0.30		1.75±0.12
C1 a	37:06.190	09:17.42	1.38	0.48	42.7	24.02±0.04	1.583	2.52±0.06
b	37:06.466	09:24.80	1.14	0.63	10.1	24.19±0.05		2.29±0.06
c	37:07.515	09:39.42	0.84	0.48	41.1	24.94±0.07		1.62±0.04
C2 a	37:07.024	09:33.73	0.75	0.39	67.1	25.59±0.15	[1.39 ± 0.08]	3.09±0.06
b	37:06.724	09:31.05	0.60	0.24	38.6	25.57±0.16		2.80±0.05
[c]	[37:05.822]	[09:12.94]				[26.4]		1.83±0.08
C15 a	37:04.294	09:43.41	0.42	0.21	37.3	26.00±0.18	5.421	2.74±0.08
b	37:04.861	09:51.79	0.27	0.21	39.6	26.52±0.22	5.421	2.89±0.07
c	37:05.691	10:00.41	0.39	0.24	41.6	26.07±0.17		2.69±0.10
C20 a	37:04.560	09:49.94	0.81	0.30	44.6	25.46±0.11		4.9±0.3
b	37:04.707	09:51.85	0.96	0.30	49.2	24.83±0.06		5.5±0.7
c	37:05.231	09:57.58	0.59	0.28	59.2	26.32±0.16	2.689	3.61±0.09
C23 a	37:07.894	09:29.88	0.36	0.27	39.0	26.44±0.18	3.135	2.37±0.07
b	37:07.618	09:19.99	0.42	0.21	33.7	26.80±0.23		2.57±0.06
[c]	[37:06.634]	[09:05.43]				[27.4]		1.73±0.05
Possible multiple-image system								
C10 a	37:03.672	10:16.75	1.0	0.25	55.0	24.56±0.08	[1.11±0.12]	3.5±0.6
b	37:03.458	10:15.85	1.4	0.18	107.0	25.27±0.13		3.7±2.0
[c]	[37:04.290]	[10:23.14]						
Maximum redshift of single images								
C3	37:08.203	09:22.70	1.9	0.5	108		[< 2.7]	
C5	37:06.404	09:48.42	1.1	0.4	154		[< 2.7]	
C9	37:04.235	10:01.67	1.7	0.3	146		[< 2.3]	
C11	37:04.789	10:03.60	1.2	0.6	152		[< 1.9]	
C13	37:04.498	10:28.08	2.6	0.4	115		[< 1.5]	
C18	37:07.945	09:31.83	1.2	0.4	114		No Constraints	

Table 3: Properties of the multiple-image systems. In addition to the 6 secured systems, C10 is included as a potential candidate (see Sect. 3.1). From left to right: identification, astrometric position (J2000), ellipse shape parameters (a, b, θ), R_{702W} magnitude, measured redshift, magnification factor (in magnitudes) derived from the mass model. Bracketed values are also predictions inferred from the mass model.

^aSmith et al. (2002b)

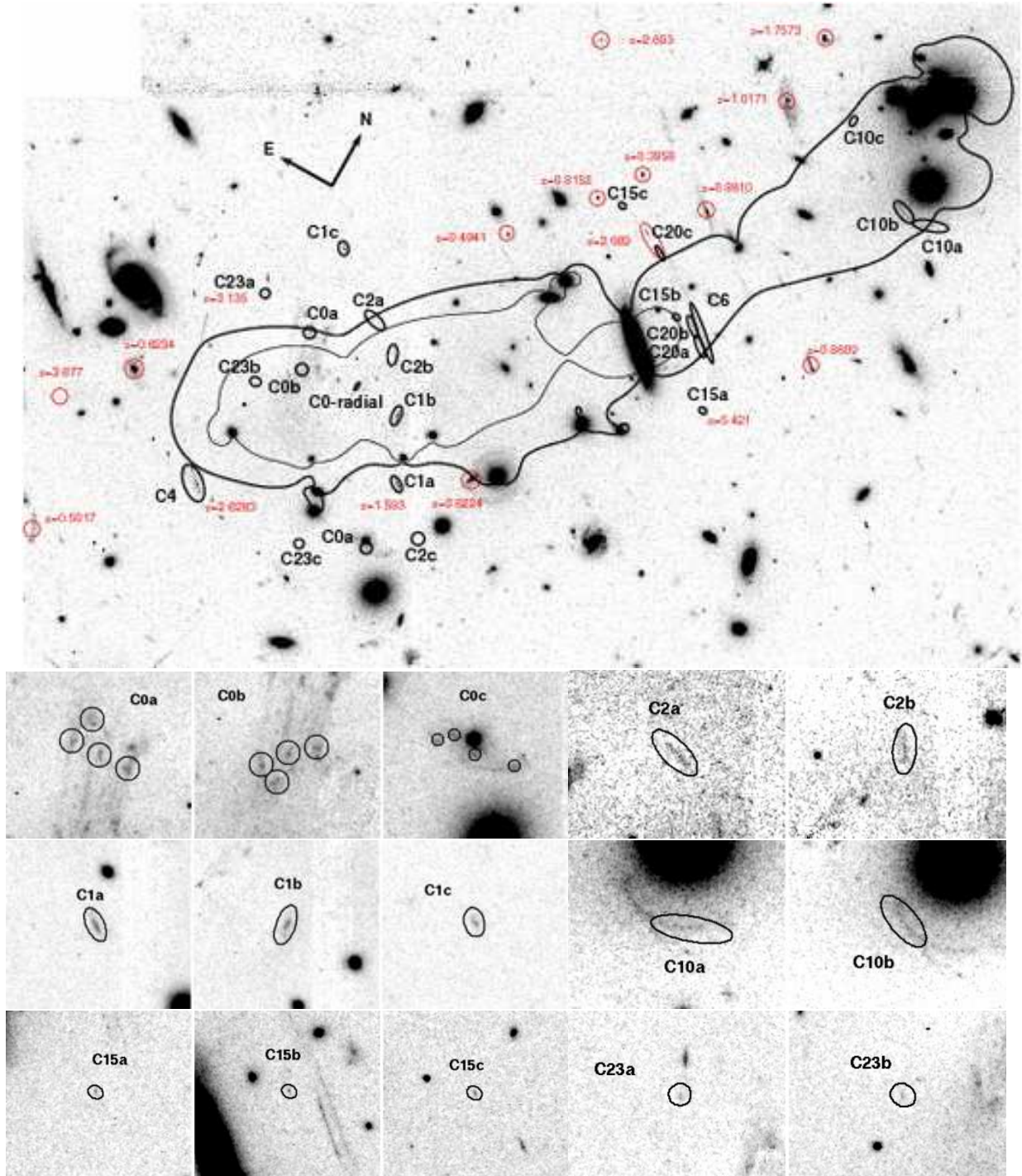


Fig. 3.— (Top) Enlarged region of the R -F702W image showing the location and morphology of the multiple-image systems identified in the field of Abell 68. We subtracted the contribution from the brightest cluster galaxy (BCG) to assist in the identification of underlying objects, such as the radial arc associated with C0. The thin/thick black curves show the location of the critical lines at $z = 1.6$ and $z = 5.42$ respectively, as inferred from the mass model (§4). We overplot in red new spectroscopic redshifts of background sources. (Bottom) Close-up on each component of the multiple systems discussed in the text.

of red $(R - I)_{AB} \sim 1.7$ and blue $(I - z)_{AB} \sim -0.5$ colors, as measured with aperture photometry on the seeing-matched images. Such a spectral energy distribution (SED) is characteristic of galaxies in the redshift range $5 \lesssim z \lesssim 6$, where the Lyman- α break in the spectral continuum occurs between the R and I bands. The preliminary mass model (§4) shows that the location of these three images is compatible with a multiply-imaged source, thereby strengthening the high redshift interpretation. We designate this system by C15 (with three images C15a,b,c that correspond to C15/16/17) and confirmed the components C15a and C15b lie at the same redshift using LRIS spectroscopy (see Section 3.2).

The arclet identified as C20 was serendipitously covered during the same LRIS long-slit observation. We interpret the extended emission seen in the spectrum (Sect. 3.2) as Lyman- α at $z = 2.689$. This is also supported by the mass model, which predicts 2 detected counter-images with similar optical colors. We refer to this system as C20a,b,c.

Next to C20a and C20b images, a fainter extended arc C6 was identified by S05 as a possible multiply-imaged system at a similar redshift. This arc can be split into 3 components C6a,b,c.

Finally, we uncovered a new lensed image, C23a, close to the cluster center during the critical line survey using LRIS (Santos et al. 2004). Its spectrum is consistent with a high redshift source dominated by its Lyman- α emission. Again, the cluster mass model predicts the position of a second faint component for this system (C23b), detected on the HST image.

3.2. Redshift Constraints

We now present the new spectroscopic redshifts obtained for 6 multiply-imaged candidates, as well as constraints implied for the remaining multiply-imaged systems C2 and C10, from the updated mass model (Sect. 4).

- C0 source

This source is a strongly-lensed ($\mu \sim 3.2$ mag.) multiply-imaged system with three components, discovered during a survey for Extremely Red Objects (EROs) in the fields of 10 massive galaxy cluster lenses at $z \sim 0.2$ (Smith et al. 2002a). A redshift measurement on the brightest image, C0a, was presented in Smith et al. (2002b). Based on the 4000 Å-break identification at $\lambda = 1.04 \pm 0.01 \mu\text{m}$, the redshift is $z = 1.60 \pm 0.03$. This image was also included in two LRIS masks, but we failed to detect strong spectral features in the wavelength range 5500-9200 Å .

Because of the clear symmetry of images C0a and C0b with respect to the critical line, it is possible to isolate 4 bright knots in each image a , b and c and use the corresponding 12 images to constrain the mass model. Furthermore, part of the south-west knot of C0a is located within the radial caustic line in the source plane. We are able to detect a very faint radial arc predicted by the mass model (labeled C0-radial on Fig. 3) after removing the light from the BCG.

- C1 source

The brightest component C1a of this system was observed during our NIRSPEC critical lines survey (see Stark & Ellis (2006) and Stark et al. (2006b), in press). Three strong emission lines were identified as $[OIII]5007$, $[OIII]4959$ and $H\beta$ (Figure 4, left), which unambiguously give a redshift $z = 1.583$. Optical spectroscopy of component C1c, included in one of our LRIS masks, could not identify any

strong $[O_{II}]$ emission for this source, with a 3σ upper limit of 50 \AA for the equivalent width in rest-frame.

- C4 source

Although not multiply-imaged, this blue arc has very strong Lyman- α emission corresponding to $z \sim 2.63$. An extended Lyman- α blob has also been detected in the IFU data (see Sect. 5.4 and Figure 3). The mass model gives a very high magnification factor of $\mu \sim 4.0$ mag., because the source is very close to a cusp.

- C6 and C20 sources

We identify a spatially-extended emission line in the LRIS spectrum at $\lambda = 4485 \text{ \AA}$, surrounding the C20c image (Fig. 4, middle). The lack of other strong emission lines in the optical range and the predicted position for two other components for C20 from the mass model confirms this to be Lyman- α at $z = 2.689$. In addition, this redshift is close to the Lyman- α blob associated with C4, and we identify a similar strong emission line at a similar redshift, $z = 2.693$, for the nearby source C25 ($\sim 8''$ away in the source plane).

The location and color of the lower surface brightness arc, C6, close to images C20a and C20b, is compatible with three merging images forming a single giant arc at a similar redshift (Fig. 4, middle). This is further evidence of a possible group of galaxies at $z \sim 2.6$ including sources C6, C20 and C25.

- C15 source

A strong asymmetric emission line is clearly seen on the LRIS spectrum at the position of C15a and C15b (Figure 4, top-right), with a central peak at 7808 \AA . In both cases, a faint continuum is detected on the red side of the emission line, with a flux $\sim 4.4 \pm 1.5 \times 10^{-19} \text{ ergs s}^{-1} \text{ cm}^{-2} \text{ \AA}^{-1}$. We interpret the emission line as Lyman- α at $z = 5.421$. This redshift could be slightly overestimated due to an unknown amount of self-absorption in the Lyman- α emission line and the absence of other spectral features. By averaging the extracted spectra of both images (Figure 4, top-right), the integrated flux measured within the emission line, of $9.7 \pm 0.8 \times 10^{-17} \text{ ergs s}^{-1} \text{ cm}^{-2}$, corresponds to a rest-frame equivalent width of $\sim 35 \text{ \AA}$. We measure a Full-Width Half-Maximum of $\sim 7 \text{ \AA}$ when fitting the average emission line with a gaussian profile. The strong Lyman- α emission line of this source seems to dominate the overall I -band flux.

- C23 source

The identification of the pair of images C23a and C23b, predicted by the lensing model at $z = 3.1$, strengthens the Lyman- α interpretation for the single emission line seen in the spectrum of C23a at $\lambda = 5028 \text{ \AA}$. A fainter counterimage, C23c, predicted by the mass model, lies beyond the detection limit of the HST image.

- C2 source

This system is composed of two bright symmetrical images, identified close to the cluster center. Using the mass model, we predict a redshift of $z \sim 1.4$ for this source, with a magnification factor of $\mu \sim 2.9$ mag. for C2a and C2b. A less magnified ($\mu \sim 1.8$ mag.) counter-image C2c is also predicted by the model, but is not detected in the less-sensitive region of the HST image, at the junction between 2 WF chips.

- C10 source

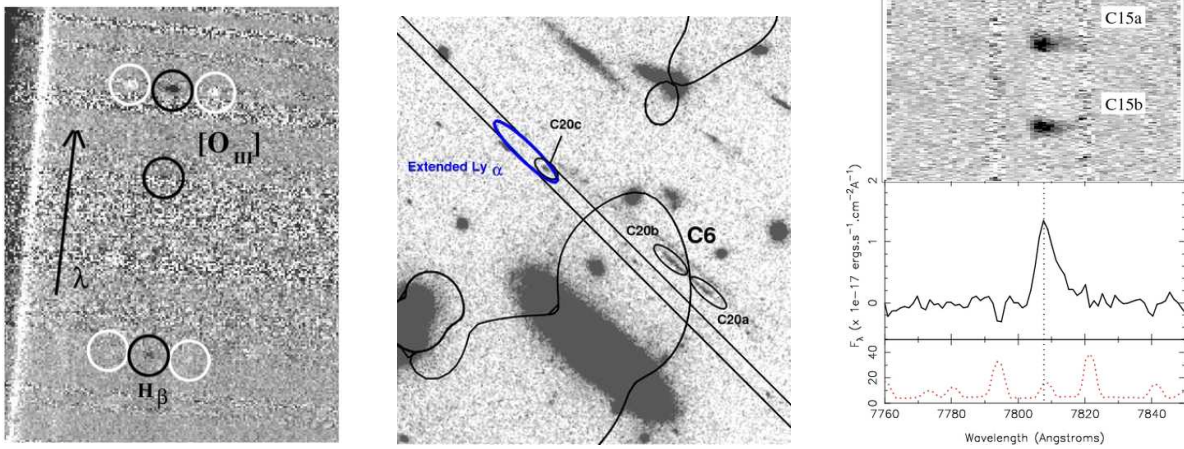


Fig. 4.— (Left) NIRSPEC bidimensional spectrum of component C1a, showing the detection of 3 strong features identified as $[O_{III}]$ and H_{β} emission lines at $z = 1.583$, both in positive (black) or negative (white), due to dithering offsets used. (Middle) Location of the LRIS slit and extended Lyman- α emission identified around image C20c (thick ellipse). Two brighter components C20a and C20b are predicted by the mass model, in agreement with the location of the critical line at $z = 2.68$ (solid curve). The shape and colors of the adjacent giant arc C6 are compatible with a similar redshift, suggesting a physical connection between these two sources. (Right) Upper panel: close-up of the 2-D sky-subtracted LRIS spectrum, showing both strong emission lines seen at the position of C15a and C15b. Lower panel: average extracted spectrum of C15, with the same wavelength range, revealing the clear asymmetrical shape of the spectral line. The relative sky background level is presented as a dotted curve.

A faint curved arc near a bright cluster member was identified by S05 as a multiple imaged candidate C10. The optical colors of this blue arc are indeed compatible with a source at $z < 2.5$. It is probably formed by two images merging on the critical line; its shape is in agreement with predictions from the mass model. However, the low surface brightness of this arc and the lack of spectroscopic information strongly limit this interpretation, making it more uncertain than the systems previously mentioned. Therefore, we only include this source in Table 3 as a possible additional multiple imaged system. The mass model predicts a redshift of ~ 1.1 which is in very good agreement with the photometric redshift estimate of $z_{phot} = 1.15 \pm 0.05$ derived from the broad band colors using the *Hyperz* photometric redshift code (Bolzonella et al. 2000). A fainter counter-image (C10c) is predicted by the mass model, but remains undetected in the HST image.

4. Mass model

4.1. Modeling method

Using the new redshift measurements and the identification of further multiply-imaged systems, we are now in a position to considerably improve the precision of the mass model presented by S05. In doing so, we will maintain the Pseudo-Isothermal Elliptical Mass Distribution model (PIEMD, Kassiola & Kovner 1993) adopted by S05 to infer the dark matter mass distribution. This parametric method has been used for modeling galaxy clusters as well as individual galaxies (Covone et al. 2006; Natarajan et al. 1998). It assumes each dark matter clump can be parameterized by a central position, ellipticity a/b , position angle θ , central velocity dispersion σ_0 and two characteristic radii r_{core} and r_{cut} . The total mass of this profile is proportional to $r_{cut} \sigma_0^2$. A more detailed discussion of the validity of this approach, in contrast to alternatives, is given by Limousin et al. (2007).

The cluster galaxy population is incorporated into the lens model as galaxy-scale perturbations to the cluster potential, assuming a scaling relation $M/L = \text{Const}$ (Brainerd et al. 1996, S05) for all the r_{core} , r_{cut} and σ_0 . This is motivated by the similar Faber & Jackson (1976) scaling relation observed in elliptical galaxies. Following the same procedure as Limousin et al. (2007), we keep the r_{cut}^* and σ_0^* values corresponding to a L^* elliptical galaxy as free parameters, while keeping r_{core}^* at 0.15 kpc. We select cluster galaxies in the field of Abell 68 by plotting the characteristic cluster red sequences ($B-R_{702}$) and ($R_{702}-K$) in two color-magnitude diagrams, keeping the objects pertaining to both red sequences. This reduces the photometric catalog used by S05, containing 69 galaxies with K band photometry, to 47 cluster members. This method is more efficient than a single red sequence selection as we did not select any of the spectroscopically confirmed background or foreground galaxies. As described in S05, the K -band photometry was obtained by Balogh et al. (2002) using GIM2D (Simard 1998) to fit the surface brightness profiles of the cluster galaxies. This method gives more accurate results than one could obtain with SExtractor, because SExtractor usually overestimate the local background around the brightest and most extended galaxies.

In a first attempt at modeling the lens, we adopted the parameters given by S05, who included two dark matter halos. We found any attempt to reconstruct the mass distribution using a single clump was unable to reproduce the multiply-imaged systems accurately, confirming the strong bimodality of this cluster. By incorporating our spectroscopically-confirmed multiply-imaged systems, a reoptimization is necessary. To do

this, we use the new bayesian optimization method provided by the *Lenstool* software²(Kneib 1993, Jullo et al. in prep.) so that we can derive error estimates for each optimized parameter. The software optimizes the locations of each system in the source plane, based on the following χ^2 estimator, which defines the goodness of the fit:

$$\chi^2 = \sum_i \chi_i^2 \quad (1)$$

where χ_i^2 is the same estimator for a given multiply-imaged system i , constructed by comparing the predicted positions of the N observed images in the source plane $(x_{i,j}, y_{i,j})$ to their barycenter (x_i^B, y_i^B) :

$$\chi_i^2 = \frac{1}{N} \sum_{j=1..N} \frac{(x_{i,j} - x_i^B)^2 + (y_{i,j} - y_i^B)^2}{\sigma_{pos}^2} \quad (2)$$

σ_{pos} is the uncertainty in measuring the position of each image in the source plane. We use a typical value of $\sigma_I = 0.2''$ for the same uncertainty in the image plane, and relate it to σ_{pos} with the amplification A : $\sigma_I^2 = A \sigma_{pos}^2$.

For its important influence on the position of systems C15 and C20, we choose to optimize the velocity dispersion and the cut radius of the third brightest cluster galaxy. We also optimize the same parameters for the BCG and the galaxy #106 (adjacent to image C0c), in order to match the location of all images from the C0 system.

The associated reduced χ^2 is ~ 1.7 , with 21 degrees of freedom, and the astrometric error on the position of the predicted multiple images is $0.37''$ in the image plane. The new parameters of the mass model are presented in Table 4. The optimized values are slightly higher than the ones we obtain by using only their luminosity as a parameter for the gravitational potential. However, those values are not sufficiently high to propose a third dark matter clump. As additional confirmation for the quality of the mass model, we also checked that all spectroscopically-confirmed background sources for which we did not identify multiple-image systems were predicted to be singly-imaged.

In comparison with the results from S05, we have refined the mass model by increasing the number of constrained parameters from 11 to 21, while keeping a similar reduced χ^2 value. In particular, we optimized the location of the second dark matter clump, where we have the main differences in the confirmed multiply imaged systems, and constrained individual parameters for two particular galaxies, in complement to the BCG.

4.2. Results from the Mass Model

Our improved mass model of Abell 68 enables us to compute a *lensing* mass of the cluster by integrating the derived surface mass density within a given projected distance R . Within a physical radius $R < 500$ kpc, we obtain a value $M_{lensing} = 5.31 \pm 0.17 \times 10^{14} M_\odot$. This is somewhat higher than the value of $4.4 \pm 0.1 \times 10^{14} M_\odot$ derived by S05. By comparing both models using the individual parameters given in table 4, this difference arises mainly because of the higher mass of the second dark matter clump, for which we derive higher σ_0 and r_{cut} values compared to S05. The remaining model parameters (the location, ellipticity and orientation) lie within 3σ . We argue that the parameters of the secondary clump are better constrained in our model, given the identification of new multiple images to the NW of the cluster. The difference

²For more information and to download the latest version of the code, see <http://www.oamp.fr/cosmology/lenstool>

with S05 is further revealed by computing the ratio M_{cen}/M_{tot} between the mass of the central component (with sole contributions from the main clump and the BCG) and the total mass within 500 kpc. We find $M_{cen}/M_{tot} = 0.56 \pm 0.05$, lower than the value of 0.68 derived by S05. This strengthens the bimodal nature of Abell 68. Our parameters for the individual contributing galaxies are quite similar to S05, except for the low r_{cut}^* value, indicating that the haloes have a smaller spatial extent.

Within the uncertainties, we are now able to predict the location and expected fluxes of the counter-images for the observed multiple systems C2, C10 and C23. Furthermore, the model gives us an estimate of the redshift for the multiple systems C2 and C10 which do not yet have spectroscopic measurements. These predictions are summarized in Table 3 as bracketed values.

In the process of the bayesian optimization, the software computes the magnification factors and the related error estimates, for each source included in the spectroscopic catalog or the multiple images catalog. These values are reported in Table 2 and 3, respectively.

Apart from the multiple-image systems described before, all other background sources in our spectroscopic catalog (C4, C7, C8, C12, C14, C24, C25, C26, C27) are predicted to be singly-imaged. This is compatible with our morphological data. For other sources that do not show multiple images (C3, C5, C9, C11, C13, C18), we use the mass model to predict their maximum redshift z_{max} . As the radius of the critical line increases with source redshift z_s , a multiple image is expected if $z_s > z_{max}$. These z_{max} values are summarized in Table 3 and are consistent with the observed optical colors. Image C18 is predicted to be a single image at any redshift.

5. Physical Properties of Faint Lyman- α Emitters

Via our spectroscopic campaign and improved mass model, we are now in a position to explore the physical properties and luminosity distribution of a large sample of intrinsically faint $2 < z < 6$ sources. We recognize that the volumes sampled may be unrepresentative but that our survey illustrates, by example, the promise of more extensive surveys that may soon be possible with larger cluster samples.

First we selected from our spectroscopic catalog a subsample of seven high redshift sources ($z > 1.5$), which all have clearly detected Lyman- α emission lines. The measured rest-frame equivalent widths W exceed 2 \AA , and the majority have $W \gtrsim 10 \text{ \AA}$. By contrast, typical LAEs selected within narrow-band surveys have $W \gtrsim 30 \text{ \AA}$. The strong magnification thus gives us insight into the physical properties of these

Mass component	$\Delta R.A.$ (arcsec)	ΔDec (arcsec)	a/b	θ (deg)	r_{core} (kpc)	r_{cut} (kpc)	σ_0 (km s^{-1})
Cluster#1	-1.5 ± 0.4	0.2 ± 0.3	1.8 ± 1.0	125.9 ± 0.6	87.9 ± 6.0	1239 ± 471	908 ± 37
Cluster#2	-48.4 ± 1.6	63.2 ± 2.2	[1.0]	[0.]	65.1 ± 14.3	1350 ± 281	757 ± 57
BCG	[0.]	[0.]	[1.3]	[122.5]	[0.25]	83 ± 45	266 ± 5
#3	[-27.5]	[22.]	[2.6]	[53.9]	[0.043]	150 ± 34	179 ± 7
#106	[-10.0]	[-14.5]	[1.2]	[0.]	[0.013]	188 ± 63	63 ± 7
L^* elliptical galaxy	–	–	–	–	0.15	18 ± 5	179 ± 13

Table 4: Most likely parameters of the lens model with 1σ error bars. From left to right: identification, astrometric position relative to the Brightest Cluster Galaxy, PIEMD parameters. θ orientation is increasing from north through east. Bracketed values are not optimized.

faint LAEs, including the star formation rate, the stellar mass and the physical scale corresponding to the star-forming regions. These physical values are derived and summarized in Table 5.

5.1. Star Formation Rates

We explore two ways of determining the instantaneous star formation rate (SFR) for a high redshift LAE, both using the calibration from Kennicutt (1998) who assumed a Salpeter (1955) initial mass function with mass limits 0.1 and 100 M_{\odot} . The first calibration is based on the UV continuum luminosity L_{1500} , at 1500 Å in rest-frame, with the following relationship:

$$SFR_{UV}(M_{\odot} \text{ yr}^{-1}) = 1.05 \times 10^{-40} L_{1500} (\text{ergs s}^{-1} \text{ \AA}^{-1}) \quad (3)$$

We estimated the individual L_{1500} values in this sample through the broad-band photometric measurements.

The second calibration adopted from Kennicutt (1998) is based on the intrinsic luminosity within the Lyman- α emission line, assuming no extinction and case B recombination (Brocklehurst 1971) :

$$SFR_{Ly\alpha}(M_{\odot} \text{ yr}^{-1}) = 9.1 \times 10^{-43} L_{Ly\alpha} (\text{ergs s}^{-1}) \quad (4)$$

The corresponding SFR estimates are given in Table 5.

In most cases, we find good agreement between these two estimates, with a trend for $SFR_{Ly,\alpha}$ to be lower than SFR_{UV} , with a mean ratio $SFR_{UV}/SFR_{Ly\alpha} \sim 1 - 4$. We interpret this difference as due to the specific properties of Lyman- α emission, which usually show some self-absorption or dust extinction. The ratio above is quite similar to that, ~ 3 , typically found in high-redshift Lyman- α samples (Santos et al. 2004; Ajiki et al. 2003), as well as for the most distant galaxies at $z \sim 6.5$ (Hu et al. 2002; Kodaira et al. 2003). We notice two exceptions for C27 and C25; these show much higher SFR ratios (~ 50). Since C27 shows a double-nucleus, its UV emission may be coming from an AGN. For C25, we estimate a 0.6''-offset between the center of the star-forming region and the center of the LRIS slit (originally aligned on C15a and C15b). Conceivably we missed the majority of the light coming from this object, which may explain the discrepancy.

5.2. Stellar Masses

Next we combine the constraints from multiband photometry and spectroscopic redshifts to derive estimates of the stellar mass associated with each source. A key question is whether LAEs are being seen at a special stage in their evolution, for example with a high star formation rate but low stellar mass. In this calculation, prior to SED fitting, it is important to remove the contribution of the Lyman- α flux from the photometric measurements.

We derive the stellar mass using the Bayesian stellar mass code developed by Bundy et al. (2005), which compares the SED of each object with a grid of synthetic SEDs from Bruzual & Charlot (2003), assuming

a Chabrier (2003) Initial Mass Function. The star-formation history is parametrized as an exponential decaying burst $SFR \propto \exp -t/\tau$. In addition, the code gives an error estimate for each stellar mass, combining photometric errors and degeneracies in the model parameter space (age, reddening, metallicity, star-formation history). At $2 \lesssim z \lesssim 5.5$, photometric measurements or upper limits in the 7 filters from Table 2.1 cover the restframe UV and optical wavelengths, which is the main limiting factor in deriving stellar masses. Depending on the number of photometric bands (2 to 7) where a LAE is detected, the typical errors arising from the degeneracies in model parameters cover the range 0.1 to 0.5 in $\log_{10}(M_*)$. It was not possible to derive a stellar mass for C26, because it is only detected in the R_{F702W} filter.

Stellar masses, corrected for magnification, are reported in Table 5. We also compute the inverse of the specific star formation rate (star formation rate per unit stellar mass, Brinchmann et al. (e.g. 2004)) based on the SFR_{UV} estimate. This gives an indication on which timescale the star formation is taking place in each object. We find typical values of 500 Myr to 1 Gyr, suggesting that higher star formation may have occurred in these LAEs during the past, unless they were formed very early.

5.3. Physical scales

In addition to brightening the observed flux of background sources, the magnification also stretches the angular sizes of the lensed images. This affects all the object shape parameters (a , b , θ), increasing the observed solid angle by the same factor μ . We are thus able to probe a physical scale R in the source plane, with:

$$R = \sqrt{\frac{a b}{\mu}} D_A(z) \quad (5)$$

where $D_A(z)$ is the angular distance for a source at z .

For most of the high redshift sources which are not resolved (along one direction) in the HST image, this value of R is an upper limit (Table 5). In most cases, we find that we are able to probe high redshift sources at sub-kiloparsec scales. Another interesting physical property we derive is the intrinsic surface density of star formation ($\Sigma = SFR_{UV}/(\pi R^2)$), which is a lower limit when sources are unresolved.

5.4. Lyman- α emission surrounding C4

We now turn to a specific issue relating to the origin of the so-called Lyman- α blobs, of which C4 at $z = 2.63$ is the first lensed example. We have used the updated mass model to reconstruct the source-plane morphology of C4. The high magnification (~ 4 mags.) enables us to resolve the source morphology at ~ 30 pc scales. The galaxy displays a bright component with an intrinsic elongated shape and several knots, at a scale length of ~ 3 kpc along the major axis. A fainter component having a similar shape and one bright knot is located ~ 4.6 kpc away (Fig. 5, fourth panel). Such an elongated shape and small physical scale is not uncommon among high redshift galaxies: Ravindranath et al. (2006) have measured that $\sim 50\%$ of galaxies in their sample of $z > 2.5$ LBGs taken from GOODS show a bar-like morphology, and scale lengths of about 1.7 – 2. kpc.

The strong Lyman- α emission of C4 detected with LRIS was also identified in the VIMOS/IFU data

	C27	C4	C20c	C25	C23a	C26	C15ab	Ellis et al.
z	1.75	2.63	2.69	2.69	3.13	3.68	5.42	5.58
μ (mags)	1.72	4.15	3.61	1.12	2.37	2.06	2.79	3.80
L_{1500}^a	6.1	5.5	0.41	4.6	0.39	0.24	3.68	0.21
$f_{Ly\alpha}^b$	4.6±0.6	9.3±0.6	4.8±0.4	1.3±0.5	1.5±0.3	2.6±0.2	9.7±0.8	6.8±0.7
$L_{Ly\alpha}^c$	2.1±0.3	1.6±0.1	1.4±0.1	2.9±1.1	1.4±0.28	3.4±0.3	29±2.4	6.9±0.7
SFR_{UV}^d	6.4	5.8	0.44	4.8	0.41	0.25	3.9	0.22
$SFR_{Ly\alpha}^d$	0.19±0.03	0.15±0.01	0.13±0.01	0.26±0.09	0.13±0.03	0.31±0.03	2.62±0.22	0.35±0.04
$\log_{10}(M_*/M_\odot)$	9.6 ± 0.1	8.7 ± 0.2	8.4 ± 0.3	9.7 ± 0.1	8.6 ± 0.5	N/A	9.4 ± 0.3	8.2 ± 0.2
R (kpc)	2.8	2.2	< 0.36	< 0.72	< 0.37	< 0.34	< 0.28	< 0.19
Σ^e	0.25	0.38	> 1.08	> 2.94	> 0.95	> 0.68	> 15.8	> 1.93
M_*/SFR^f	6.2	0.9	5.7	10.4	9.7	N/A	6.4	7.2

Table 5: Summary of physical properties derived for all LAEs at $z > 1.5$ in our sample, and comparison with the mean values of the source at $z \sim 5.6$ found by Ellis et al. (2001) in Abell 2218 (rightmost column). From top to bottom: redshift, magnification factor μ , unlensed UV luminosity (L_λ) at rest-frame $\lambda = 1500 \text{ \AA}$, observed integrated flux in the Lyman- α emission line, corresponding unlensed Lyman- α luminosity, star formation rate derived from the UV continuum (SFR_{UV}) or the Lyman- α emission ($SFR_{Ly\alpha}$), stellar mass estimate from SED fitting (see Sect. 5.2), intrinsic physical scale R (see Sect. 5.3), star formation surface density Σ and specific star formation rate.

- ^a $\times 10^{40} \text{ ergs s}^{-1} \text{ \AA}^{-1}$
^b $\times 10^{-17} \text{ ergs s}^{-1} \text{ cm}^{-2}$
^c $\times 10^{41} \text{ ergs s}^{-1}$
^d $M_\odot \text{ yr}^{-1}$
^e $M_\odot \text{ yr}^{-1} \text{ kpc}^{-2}$
^f $\times 10^8 \text{ yr}$

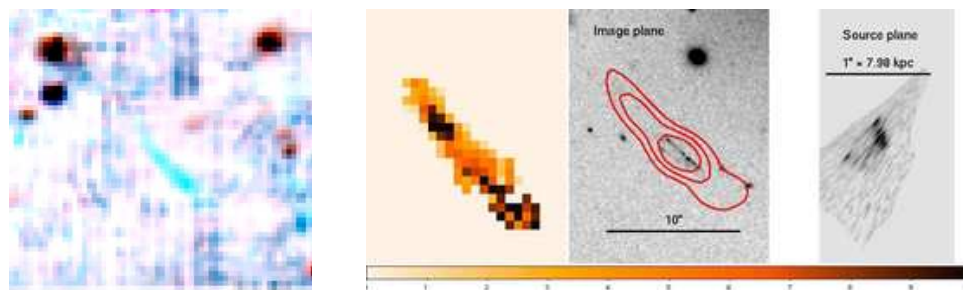


Fig. 5.— (Left) Negative color image of a $40''$ side region around the source C4, produced by combining three different wavelength slices from the IFU datacube : a 15 \AA -wide region encompassing the Lyman- α emission (blue), and two broad wavelength regions at redder wavelengths (green and red). The extended emission around the arc C4 is clearly detected in the blue frame.

(Right) Lyman- α emission properties of C4 observed with the IFU data. From left to right: rest-frame equivalent-width mapping of the Lyman- α emission (with corresponding color-scale), contours of Lyman- α emission overplotted on the HST image, R -band reconstruction of C4 in the source plane.

(Fig. 5, first panel). Compared with the observed size of the arc in the continuum image R_{702} ($4 \times 1.2''$) this emission is significantly more extended ($\sim 15 \times 3''$, third panel of Fig. 5). After correction for an average magnification, this corresponds to an intrinsic scale of ~ 10 kpc.

We use the R_{702W} image to estimate the continuum flux of C4 at the wavelength of the Lyman- α emission, after applying a k -correction factor assuming a UV spectral slope of 2.0 typical of starburst galaxies. By comparing the spatial coverage of the Lyman- α emission and the continuum, we construct a map of rest-frame Lyman- α equivalent width W_0 (Fig. 5, second and third panel). The W_0 values are typically in the range $5 < W_0 < 10 \text{ \AA}$ in the region detected on the HST image. However, the map shows a significant increase of Lyman- α equivalent width, with values $W_0 > 10 \text{ \AA}$, in the northern part of the arc, where the continuum is hardly visible in R band. Because of the size of the blob and the presence of this stronger stellar continuum at the center of C4, the most probable mechanism producing such an extended Lyman- α emission is the presence of a superwind outflow originating from the central starburst Taniguchi et al. (2001); Wilman et al. (2005).

We also observed C4 with 2 different LRIS configurations, located across or along the longer dimension of the arc (Fig. 6). In both cases, we observed two different components to the Lyman- α line on the 2D spectrum : a stronger emission centered around 4411 \AA and a fainter emission region at a slightly bluer wavelength (4408 \AA). The LRIS data also shows a tilt in the emission region, due to an offset in the central peak of the Lyman- α line (top panel of Fig. 6). These components may be related to the different star-forming regions identified morphologically in the HST image. Unfortunately, because of the poorer resolution, no similar offset in the central wavelength or variations in the line profile were detected in the IFU data.

The main difference between C4 and the very luminous Lyman- α blobs is its very small physical size : 2.2 kpc, compared with the $R > 30$ kpc selection criteria for Lyman- α blobs adopted by Matsuda et al. (2004), along with the rest-frame equivalent width criterion $W_0 > 20 \text{ \AA}$. For this reason, it is more likely that the associated physical processes may be different, the size of C4 being more similar to extended Lyman- α emissions observed around star-forming galaxies. In this strongly lensed case, the effects of outflows on the Lyman- α emission can be studied in higher details by way of the lensing magnification, stretching the observed scales.

5.5. Intrinsic properties of the $z = 5.4$ source

We finally turn to the most distant lensed source, C15, at $z = 5.4$, and whether it is a further example of the intriguing lensed source detected at $z=5.6$ by Ellis et al. (2001) in Abell 2218.

C15 has an intrinsic Lyman- α luminosity of $\sim 3 \times 10^{42} \text{ ergs s}^{-1}$. This is about 5 times fainter than typical values found for $z \sim 5.7$ LAEs targeted by narrow-band searches (Hu et al. 2004; Shimasaku et al. 2006), but not too dissimilar to those in the much fainter $z \sim 6.5$ sample from Kashikawa et al. (2006) who used very deep (~ 10 ks) spectroscopy with Keck and Subaru to confirm 17 faint LAEs.

All three images of this source are unresolved along the shear direction, and therefore suggest a very small physical scale $R \lesssim 300 \text{ pc}$ in the source plane. More interestingly, we infer a minimum star formation surface density of $\sim 16 M_\odot \text{ kpc}^{-2}$, which is much higher than for any other object in our sample, making this source similar to the most active star forming regions at any redshift.

The strong Lyman- α emission dominates the optical flux and in this respect it is very similar to the $z \sim$

5.6 object found by Ellis et al. (2001) in the cluster Abell 2218. To compare these sources, we have performed a re-analysis of the photometric data for that object, taking into account HST data that arrived for Abell 2218 subsequent to the Ellis et al. (2001) analysis. This includes HST/ACS, NICMOS and Spitzer/IRAC observations presented by Kneib et al. (2004) and Egami et al. (2005). We find that the Ellis et al source is now detected in the I_{F814W} , z_{F850LP} , J_{F110W} and H_{F160W} filters (Fig. 7 and Table 6). The source is faint ($AB \sim 26.6$) and remains undetected with IRAC at 3.6 and 4.5 microns. However, the IRAC upper limits are quite high (around $AB \sim 24$), due to the proximity of the BCG ($\sim 15''$) and coarse point spread function.

In order to compare the revised data with that for C15, we compute and incorporate in the last column of Table 5 various physical properties for the Ellis et al. object alongside those for the other Lyman- α emitters. When deriving the stellar mass, we note the significant change implied by the new data ($M_* \sim 10^8 M_\odot$ c.f. $10^{6-7} M_\odot$ given by Ellis et al). The major change arises from different assumptions : in order to reproduce the observed Lyman- α emission and the non-detection of the UV spectral continuum in LRIS, Ellis et al used the STARBURST99 spectrophotometric code Leitherer et al. (1999) to derive an upper limit of 2 Myrs on the age of the source, assuming a constant SFR and no extinction.

Although the new HST photometry of this object is restricted to the rest-frame wavelength $\lambda < 2500 \text{ \AA}$, the SED fitting method used in our reanalysis should be more reliable because it is based on fewer assumptions, especially on the star-formation history. Our best SED fitting model also predicts Spitzer/IRAC continuum fluxes consistent with the non-detection of this pair in the $3.6 \mu m$ and $4.5 \mu m$ bands.

Compared with the $z \sim 5.6$ galaxy from Ellis et al. (2001), C15 is less magnified and is intrinsically more luminous and more massive, although with a similar physical size. The mass model predicts the source to be located ~ 2.4 kpc from the caustic line in the source plane. This suggests we are actually seeing a true small isolated object, since any similarly bright region close to C15 would also be highly magnified and multiply imaged.

Another difference between the two sources arises from the rest-frame UV stellar continuum, which is detected in the LRIS spectrum of the $z \sim 5.4$ source redward of the Lyman- α emission. Running the STARBURST99 code on this object in a similar way as done by Ellis et al. (2001), the upper limit on the age is much larger, typically 50 – 100 Myrs, with a constant SFR of $2.6 M_\odot \cdot \text{yr}^{-1}$. This gives a total mass of $\sim 1 - 3 \times 10^8 M_\odot$, which is closer to the SED fitting estimate, in comparison with the source in Abell 2218.

At the time of its discovery, the Ellis et al. (2001) object revealed a very small and low-mass (10^{6-7}) source at $z \sim 5.6$, which was also reported to be very young. With the new photometric reanalysis, and by finding another example of a LAE with similar size and Lyman- α flux, it is more probable that we are observing two 10^8 to $10^9 M_\odot$ objects with very different star-formation histories. The Ellis et al. source previously formed the majority of its stellar mass and is having a very young burst, whereas C15 has been forming stars for a larger time scale.

V_{F606W}	I_{F814W}	z_{F850LP}	J_{F110W}	H_{F160W}	IRAC $_{3.6\mu m}$	IRAC $_{4.5\mu m}$
> 28.14	26.94 ± 0.18	26.67 ± 0.15	26.60 ± 0.28	26.62 ± 0.33	> 24.1	> 24.3

Table 6: Broad-band photometry of the $z = 5.6$ galaxy discovered by Ellis et al. (2001), measured on the new HST-ACS/NICMOS and Spitzer/IRAC images.

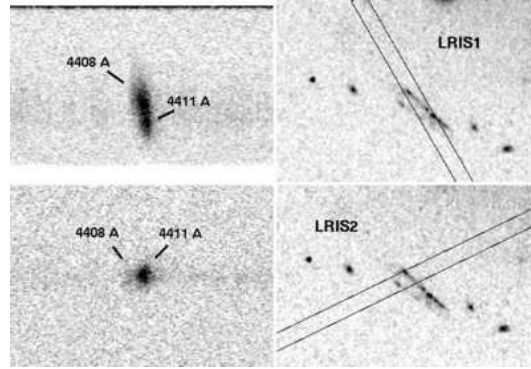


Fig. 6.— LRIS observations of C4. Left panels : closeups of each 2D spectrum showing the two components appearing in the Lyman- α emission. Right panels : corresponding LRIS slit configuration plotted over the HST image.

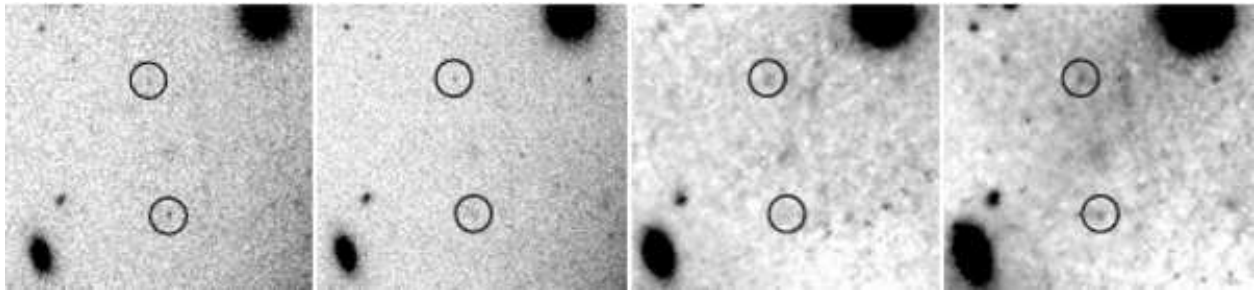


Fig. 7.— HST broad-band detections of the $z \sim 5.6$ pair found by Ellis et al. (2001) in Abell 2218. From left to right: I_{F814W} , z_{850LP} , J_{F110W} , H_{F160W} . North is up and East is left. The light from the nearby BCG (located towards the lower-right corner) has been subtracted from the NICMOS data for clarity.

6. Discussion

We have demonstrated in our survey of Abell 68 that, after applying magnification correction, we can reach LAEs with typical unlensed absolute AB magnitudes $\sim -20 < M_{\text{AB}} < -16.5$ in the rest-frame UV. This is about 2 magnitudes fainter than the UV selection criterion for typical Lyman Break Galaxies used by Steidel et al. (2003), of $R_{\text{AB}} < 25.5$ at $z \sim 3$ and the faintest LAEs found with narrow-band searches (e.g., Fynbo et al. 2003; Gawiser et al. 2006; Shimasaku et al. 2006). Moreover, the lensed Lyman- α sources have much lower equivalent widths, similar to those seen in LBGs (Shapley et al. 2003).

The derived properties of the Lyman- α emitters are dependent on the individual magnification factors μ used to correct each image for the lensing effects. The error estimates on μ , computed by the bayesian optimization method, range from 1 to 16 % and were quadratically added to the measurement errors in Table 5, in the case of $L_{\text{Ly}\alpha}$, $SFR_{\text{Ly}\alpha}$ and M_* . In each case, the photometry is the dominant source of error. We acknowledge these values of μ are still dependent on the approach used to parametrize the mass model, for instance the use of the PIEMD profile for the dark matter haloes. Nevertheless, the Lyman- α emitters presented here are strongly lensed and have been identified in the central regions of the cluster, where the magnification factors are associated with the location of the critical lines. These critical lines are constrained by the same set of multiple images, quite independently of the parametrization used for the mass model (PIEMD or Navarro-Frenk-White (NFW) profile). Therefore, we are confident that the computed magnification factors are reliable.

Although such a lensing survey is not strictly flux-limited, we can use this unique probe to gauge the properties of the faintest LAEs yet located at $z > 2$. We find the typical stellar masses are $\log_{10}(M_*/M_{\odot}) \sim 8.5$ to 9.5. These values are similar to the typical stellar masses of the bright LAEs from Gawiser et al. (2006), found by selecting very high equivalent width ($W_0 > 150$) LAEs at $z=3.1$. Our LAEs have fainter UV and Lyman- α luminosities, and therefore a lower SFR, by typically 1 to 2 magnitudes. Even if the wavelength range covered by the broad-band photometry dominates the errors in the stellar masses derived in both surveys, this is indicative that, at comparable stellar masses, our LAEs are more quiescent than the objects found in narrow-band searches.

Recognizing the limitations of our sample, as a point of illustration, we compare on Fig. 8 the luminosity range of our lensed emitters with current constraints on the cumulative Lyman- α luminosity function at $z \sim 3$, mostly based on narrow-band searches. The number of dedicated searches for LAEs at $z \sim 3$ from the literature is quite limited. We report in this diagram the compilation of 5 samples, either in blank fields or overdense environments, presented by Fynbo et al. (2001), as well as an estimate of the number density from a Ly α survey in the GOODS-south field (Nilsson et al. (2006) and Nilsson et al. 2007, to be submitted). Based on our subsample of 6 emitters at $2 \lesssim z \lesssim 3.7$ and the surface area probed in the high magnification region ($\mu > 0.75$ mag.) of the source plane, we estimate a number density of $4.3_{-1.7}^{+2.6} \times 10^{-3} \text{ Mpc}^{-3}$ down to $L = 1.4 \times 10^{41} \text{ ergs s}^{-1}$. Because our spectroscopy only sparsely covered this region, we report this value as a lower limit in Fig. 8. Although we acknowledge the limits due to very small statistics and the small areas probed in these lensed surveys, our sample of $z \sim 3$ emitters gives constraints at fainter luminosities than any of the narrow-band searches at this redshift. More observations are however needed in order to better constrain the faint-end slope of this luminosity function.

An interesting question is the likelihood of finding highly magnified sources at $z \sim 5.5$ like C15 and the source reported by Ellis et al. (2001) : we can estimate this through the space density of R -dropouts in our magnified field of view. Based on our photometric RIZ color-color selection technique (see Sect. 3.1), we identified one source in the field of view covered by the HST image. Since it is detected at $\sim 8\sigma$ level in the

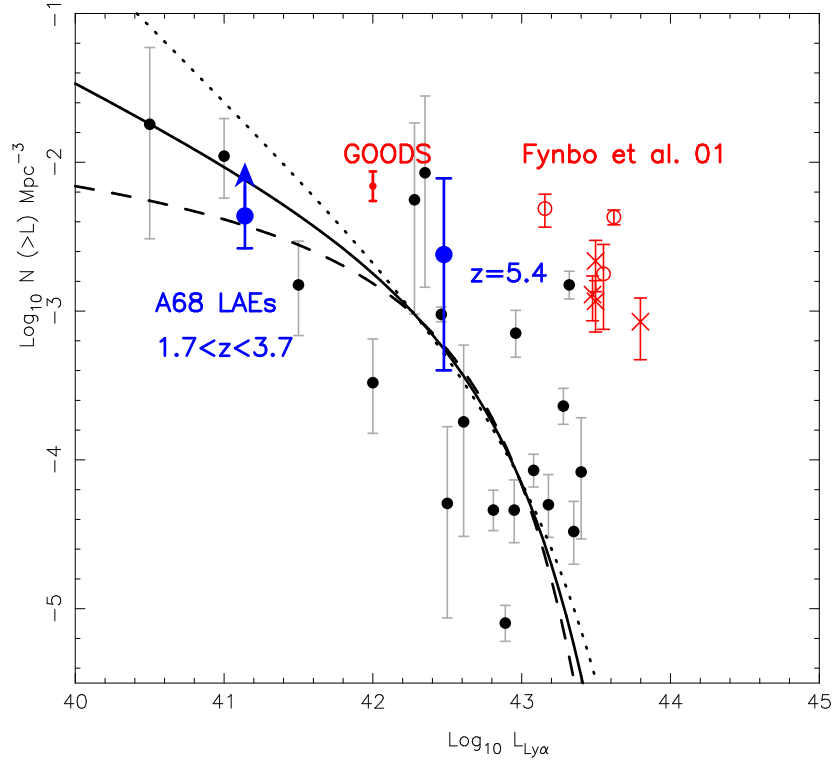


Fig. 8.— Cumulative luminosity function of Lyman- α emitters. Red datapoints are $z \sim 3$ estimates from Fynbo et al. (2001), either in overdense regions (open circles) or blank fields (crosses). We also give recent results at $z \sim 3.1$ from a Ly α survey in GOODS-South (Nilsson et al. 2007, to be submitted). Black points correspond to the compilation of $z \sim 5$ surveys from Santos et al. (2004) and black curves are more recent fits to the $z \sim 5.7$ Luminosity Function by Shimasaku et al. (2006). We overplot in blue number density estimates based on the sample of 6 Ly α emitters at $1.7 < z < 3.7$.

I -band filter, where R -dropouts are brighter, and has a magnification factor of $\mu \sim 2.5$, we computed the effective covolume in the source plane having $\mu > 0.75$, taking into account the reduction of the surface area due to lensing effects. We derive an effective covolume of 420 Mpc^3 , in the redshift range $5 < z < 6$ probed by our set of filters. Assuming Poisson noise statistics, we obtain a rough estimate of $2.4_{-2.0}^{+5.4} \times 10^{-3} \text{ Mpc}^{-3}$ for the number counts of R -dropouts. Although cosmic variance effects can be quite large when probing such a small volume, this result is in good agreement with the space density of low-luminosity Lyman- α sources at $z \sim 5$, on the above-mentioned diagram (Fig. 8).

From these simple calculations, C15 does not seem to be a serendipitous case of low-luminosity $z \sim 5$ LAE, since we would expect to find one such source in the magnified region of the cluster. By observing a larger number of lensed fields, such as the new HST clusters imaged by ACS, we could build a more significant sample of similar objects and compare their physical properties.

7. Conclusions

We have performed a spectroscopic analysis of background sources in the field of the massive cluster Abell 68 and identified 26 lensed images in the range $0.3 < z < 5.5$, including 7 Lyman- α emitters at $z > 1.7$. Using the new redshift measurements and identification of new multiple-image systems, we perform a precise modeling of the cluster mass distribution with 5 spectroscopic systems, and also predict the redshift and counter-images for two remaining systems. This makes Abell 68 one of the best-modelled lensing clusters, along with Abell 1689 and Abell 2218, allowing for the precise measurement of its dark-matter distribution.

We derived the star formation rates, stellar masses and physical scales for our sample of high-redshift Lyman- α emitters. The broad-band luminosities of these objects is comparable to the faint LAEs found in deep narrow-band searches, but their equivalent widths are much lower, making them 1 to 2 magnitudes fainter in Lyman- α luminosity. Two of these sources show a more extended Lyman- α emission region, when compared to the stellar continuum in the HST image. For one of them, we demonstrated how we use IFU data to probe regions with distinct Lyman- α equivalent widths. The stretch provided by lensing enables us to characterize small regions of Lyman- α emission which would otherwise be beyond reach of ground based Integral Field Instruments. Although the large equivalent widths are comparable to giant Lyman- α blobs observed around massive forming galaxies, we interpret the small physical scales of these lensed emissions as outflows originating from a central starburst.

The highest redshift $z \sim 5.4$ multiple-image source of this sample is very similar to the pair of strongly-lensed images identified by Ellis et al. (2001) in Abell 2218, in terms of magnification and physical size, albeit being intrinsically more massive and more luminous. We therefore expect to detect it in IRAC images of similar depth as the data presented in Egami et al. (2005), in the first two channels of this instrument. Such measurements would tighten the constraints on the stellar mass of this source, by reducing the degeneracies in the other model parameters, and also provide additional information on its age and star-formation history, when combined with the properties of the Lyman- α emission.

Our survey provides the first tentative indications of the density of faint Lyman- α emitters at $z \sim 3$, down to unlensed fluxes of $\sim 2 \times 10^{41}$. Although our survey is not flux-limited nor complete in any formal sense, the cumulative Lyman- α luminosity function we derive indicates the promise of a dedicated search for lensed Lyman- α emitters through larger samples of well-mapped clusters now being surveyed with HST, and the ability of this approach to complement narrow-band searches carried out in blank fields.

We thank the anonymous referee for his helpful comments, and acknowledge helpful discussions with Johan Fynbo, Kim Nilsson, Fabrice Lamareille, Mark Swinbank and Tommaso Treu. JR is grateful to Caltech for financial support. The Dark Cosmology Centre is funded by the Danish National Research Foundation.

REFERENCES

- Ajiki, M. et al. 2003, *AJ*, 126, 2091
- Balogh, M. L. et al. 2002, *ApJ*, 566, 123
- Bardeau, S., Kneib, J.-P., Czoske, O., Soucail, G., Smail, I., Ebeling, H., & Smith, G. P. 2005, *A&A*, 434, 433
- Bertin, E., & Arnouts, S. 1996, *A&AS*, 117, 393
- Bolzonella, M., Miralles, J.-M., & Pelló, R. 2000, *A&A*, 363, 476
- Brainerd, T. G., Blandford, R. D., & Smail, I. 1996, *ApJ*, 466, 623
- Brinchmann, J., Charlot, S., White, S. D. M., Tremonti, C., Kauffmann, G., Heckman, T., & Brinkmann, J. 2004, *MNRAS*, 351, 1151
- Broadhurst, T. et al. 2005, *ApJ*, 621, 53
- Bruzual, G., & Charlot, S. 2003, *MNRAS*, 344, 1000
- Bundy, K., Ellis, R. S., & Conselice, C. J. 2005, *ApJ*, 625, 621
- Chabrier, G. 2003, *PASP*, 115, 763
- Coleman, D., Wu, C., & Weedman, D. 1980, *ApJS*, 43, 393
- Covone, G., Kneib, J.-P., Soucail, G., Richard, J., Jullo, E., & Ebeling, H. 2006, *A&A*, 456, 409
- Czoske, O. 2002, PhD thesis, Université Paul Sabatier, Toulouse III, France
- Ebbels, T. M. D., Le Borgne, J.-F., Pello, R., Ellis, R. S., Kneib, J.-P., Smail, I., & Sanahuja, B. 1996, *MNRAS*, 281, L75
- Ebeling, H., Voges, W., Bohringer, H., Edge, A. C., Huchra, J. P., & Briel, U. G. 1996, *MNRAS*, 281, 799
- Egami, E. et al. 2005, *ApJ*, 618, L5
- Ellis, R., Santos, M. R., Kneib, J., & Kuijken, K. 2001, *ApJ*, 560, L119
- Faber, S. M., & Jackson, R. E. 1976, *ApJ*, 204, 668
- Francis, P. J. et al. 2001, *ApJ*, 554, 1001
- Franx, M., Illingworth, G. D., Kelson, D. D., van Dokkum, P. G., & Tran, K. 1997, *ApJ*, 486, L75+
- Fynbo, J. P. U., Ledoux, C., Möller, P., Thomsen, B., & Burud, I. 2003, *A&A*, 407, 147
- Fynbo, J. U., Möller, P., & Thomsen, B. 2001, *A&A*, 374, 443

- Gavazzi, R., Fort, B., Mellier, Y., Pelló, R., & Dantel-Fort, M. 2003, *A&A*, 403, 11
- Gawiser, E. et al. 2006, *ApJ*, 642, L13
- Halkola, A., Seitz, S., & Pannella, M. 2006, *MNRAS*, 372, 1425
- Hu, E. M., Cowie, L. L., Capak, P., McMahon, R. G., Hayashino, T., & Komiyama, Y. 2004, *AJ*, 127, 563
- Hu, E. M., Cowie, L. L., McMahon, R. G., Capak, P., Iwamuro, F., Kneib, J.-P., Maihara, T., & Motohara, K. 2002, *ApJ*, 568, L75
- Kashikawa, N. et al. 2006, *ApJ*, 648, 7
- Kelson, D. D. 2003, *PASP*, 115, 688
- Kennicutt, R. C. 1998, *ApJ*, 498, 541
- Kinney, A. L., Calzetti, D., Bohlin, R., McQuade, K., Storchi-Bergmann, T., & Schmitt, H. 1996, *ApJ*, 467, 38
- Kneib, J., Ellis, R. S., Santos, M. R., & Richard, J. 2004, *ApJ*, 607, 697
- Kneib, J. et al. 2003, *ApJ*, 598, 804
- Kneib, J.-P. 1993, Ph.D. Thesis
- Kneib, J.-P., Ellis, R. S., Smail, I., Couch, W. J., & Sharples, R. M. 1996, *ApJ*, 471, 643
- Kodaira, K. et al. 2003, *PASJ*, 55, L17
- Kurtz, M. J., Mink, D. J., Wyatt, W. F., Fabricant, D. G., Torres, G., Kriss, G. A., & Tonry, J. L. 1992, in *ASP Conf. Ser. 25: Astronomical Data Analysis Software and Systems I*, ed. D. M. Worrall, C. Biemesderfer, & J. Barnes, 432–+
- Le Fèvre, O., Crampton, D., Lilly, S. J., Hammer, F., & Tresse, L. 1995, *ApJ*, 455, 60
- Le Fèvre, O. et al. 2003, *The Messenger*, 111, 18
- Leitherer, C. et al. 1999, *ApJS*, 123, 3
- Limousin, M. et al. 2007, *astro-ph/0612165*
- Matsuda, Y. et al. 2004, *AJ*, 128, 569
- McLean, I. S. et al. 1998, 566
- Natarajan, P., Kneib, J.-P., Smail, I., & Ellis, R. S. 1998, *ApJ*, 499, 600
- Nilsson, K. K., Fynbo, J. P. U., Møller, P., Sommer-Larsen, J., & Ledoux, C. 2006, *A&A*, 452, L23
- Oke, J. B. 1974, *ApJS*, 27, 21
- Oke, J. B. et al. 1995, *PASP*, 107, 375
- Ravindranath, S. et al. 2006
- Richard, J., Pelló, R., Schaerer, D., Le Borgne, J.-F., & Kneib, J.-P. 2006, *A&A*, 456, 861

- Salpeter, E. E. 1955, *ApJ*, 121, 161
- Sand, D. J., Treu, T., Ellis, R. S., & Smith, G. P. 2005, *ApJ*, 627, 32
- Santos, M. R., Ellis, R. S., Kneib, J., Richard, J., & Kuijken, K. 2004, *ApJ*, 606, 683
- Scodeggio, M. et al. 2005, *PASP*, 117, 1284
- Shapley, A. E., Steidel, C. C., Pettini, M., & Adelberger, K. L. 2003, *ApJ*, 588, 65
- Shimasaku, K. et al. 2006, *PASJ*, 58, 313
- Simard, L. 1998, in *ASP Conf. Ser. 145: Astronomical Data Analysis Software and Systems VII*, ed. R. Albrecht, R. N. Hook, & H. A. Bushouse, 108–+
- Smith, G. P., Kneib, J.-P., Smail, I., Mazzotta, P., Ebeling, H., & Czoske, O. 2005, *MNRAS*, 359, 417
- Smith, G. P. et al. 2002a, *MNRAS*, 330, 1
- Smith, G. P., Smail, I., Kneib, J.-P., Davis, C. J., Takamiya, M., Ebeling, H., & Czoske, O. 2002b, *MNRAS*, 333, L16
- Stark, D. P., & Ellis, R. S. 2006, *New Astronomy Review*, 50, 46
- Steidel, C. C., Adelberger, K. L., Shapley, A. E., Pettini, M., Dickinson, M., & Giavalisco, M. 2000, *ApJ*, 532, 170
- . 2003, *ApJ*, 592, 728
- Taniguchi, Y., Shioya, Y., & Kakazu, Y. 2001, *ApJ*, 562, L15
- Wilman, R. J., Gerssen, J., Bower, R. G., Morris, S. L., Bacon, R., de Zeeuw, P. T., & Davies, R. L. 2005, *Nature*, 436, 227
- Zanichelli, A. et al. 2005, *PASP*, 117, 1271